DEVELOPMENT OF A VOLTAGE DEPENDENT CURRENT NOISE ALGORITHM FOR CONDUCTANCE BASED STOCHASTIC MODELLING OF AUDITORY NERVE FIBRE

Werner Badenhorst[1,*], Tania Hanekom[1], Johan J. Hanekom[1]

[1]Department of Electrical, Electronic and Computer Engineering, University of Pretoria, Lynnwood Road, Pretoria 0002, South Africa

*Correspondence author: Werner Badenhorst
werner.badenhorst@up.ac.za

The final publication is available at Springer via http://dx.doi.org/10.1007/s00422-016-0694-6

Abstract

The study presents the development of an alternative noise current term and novel voltage dependent current noise algorithm for conductance based stochastic auditory nerve fibre (ANF) models. ANFs are known to have significant variance in threshold stimulus which affects temporal characteristics such as latency. This variance is primarily caused by the stochastic behaviour or microscopic fluctuations of the node of Ranvier's voltage dependent sodium channels of which the intensity is a function of membrane voltage. Though easy to implement and low in computational cost, existing current noise models have two deficiencies: it is independent of membrane voltage and it is unable to inherently determine the noise intensity required to produce in vivo measured discharge probability functions. The proposed algorithm overcomes these deficiencies whilst maintaining its low computational cost and ease of implementation compared to other conductance and Markovian based stochastic models. The algorithm is applied to a Hodgkin-Huxley based compartmental cat ANF model and validated via comparison of the threshold probability and latency distributions to measured cat ANF data. Simulation results show the algorithm's adherence to in vivo stochastic fibre characteristics such as an exponential relationship between the membrane noise and transmembrane voltage, a negative linear relationship between the log of the relative spread of the discharge probability and the log of the fibre diameter and a decrease in latency with an increase in stimulus intensity.

1. Introduction

It is ever the objective of a model to represent the actual system as closely as possible whilst taking into account the required or acceptable accuracy and computational cost. A cochlear implant (CI) is a device used by profoundly deaf persons to obtain a measure of sound perception and, in particular, speech perception. These devices directly stimulate the surviving and functioning auditory nerve fibres (ANFs) with electrical pulses via an array of electrodes implanted as close as possible to the surviving ANFs inside the cochlea (Smit et al. 2009). In order to better understand and hence predict the electrically stimulated neural response (ESNR) caused by the activation of an electrode, numerous ANF models (Frijns et al. 1994; Rattay 1990; Rattay et al. 2001b; Smit et al. 2010) and volume conduction (VC) models (Frijns et al. 1995; Hanekom 2001; Kalkman et al. 2014; Malherbe et al. 2015; Rattay et al. 2001a) have been developed since the ground breaking nerve fibre model by Hodgkin and Huxley (1952). The modelled ESNRs are used to improve our understanding of the auditory nerve properties, the percepts produced by the CI and the wide variance in performance

among CI users. An improved understanding in turn allows for improved stimulation strategies and CI designs so as to ultimately improve the sound perception of the CI user (Bruce et al. 1999b; Frijns et al. 2001; Frijns et al. 1995; Macherey et al. 2007; Rattay 1989; Rattay et al. 2001a; Rattay et al. 2001b).

Because of the high frequency pulsatile stimulation of CI speech processors, the desired models not only need to estimate the neural excitation threshold or stimulus intensity value, but also the temporal characteristics (Cartee 2000; Rattay et al. 2001b). One of the important properties of a nerve fibre affecting temporal characteristics such as latency is variance in threshold stimulus intensity (Hales et al. 2004; Javel et al. 1987; Verveen 1962; Verveen and Derksen 1968). This activation threshold variability has been shown to be primarily caused by the stochastic behaviour of the node of Ranvier's sodium channels (Hales et al. 2004) or as noted by Sigworth (1980) and Rubinstein (1995): the macroscopic fluctuation of threshold can sufficiently be accounted for by the microscopic fluctuations of the voltage dependent sodium channels. The intensity of these microscopic fluctuations, also referred to as membrane noise, in turn has been shown to be a function of membrane voltage (Verveen and Derksen 1968). Numerous approaches are followed to account for the threshold variability in both conductance based (Dangerfield et al. 2012; Goldwyn and Shea-Brown 2011; Huang et al. 2013; Rattay et al. 2001b; Rubinstein 1995) and phenomenological (Bruce et al. 1999a; 1999b; Macherey et al. 2007) stochastic models. The present study focusses on conductance based models and in particular the Hodgkin-Huxley (HH) model since only these models provide biophysically meaningful results (Izhikevich 2004) as required in the study and modelling of CIs (Rattay et al. 2001b). Before reviewing the types of conductance based stochastic models that exist, it is important to first look at activation threshold variability characteristics.

The relationship between activation or discharge probability and stimulus intensity in the stochastic nerve has experimentally been shown to be Gaussian (Javel et al. 1987; Shepherd and Javel 1997; Verveen 1962; Verveen and Derksen 1968). Both the threshold (mean, μ) and spread (standard deviation, σ) of the Gaussian discharge probability function (DPF) proved dependent on stimulus duration, but the relative spread ($RS = \sigma/\mu$) was found to be independent of stimulus duration for pulse durations between 100 μs and 3 ms. *RS* thus characterises the excitability fluctuation as a measure of the threshold region width or spread (σ) relative to the mean threshold value (μ) (Rubinstein 1995; Verveen 1962). Verveen (1962) also found that *RS* decreased as the fibre diameter increased while Rubinstein (1995) further showed *RS* to be approximately proportional to $1/\sqrt{N}$ where *N* is the number of sodium channels which in turn is directly proportional to the membrane surface area *A*. Since an increase in *N* effectively results in a proportional increase in passive membrane conductance and capacitance (Rubinstein 1995), it can be stated that $RS \propto 1/\sqrt{A \cdot g_{Na}}$ where g_{Na} is the maximum sodium conductance density. This inverse proportionality results in the fibre's discharge probability becoming more deterministic as *A* increases and subsequently *RS* decreases such that log(*RS*) vs log(*A*) has a negative linear relationship (Rubinstein 1995; Verveen 1962). The decrease in *RS* as a result of the increase in the DPF gradient can also be viewed from the perspective that as the fibre diameter increases, and consequently the number of channels on a Ranvier node, the voltage fluctuation caused by a single channel becomes less significant when compared to the total ionic conductance and thus the fibre becomes less stochastic or less "noisy" (Bruce et al. 1999b; Rubinstein 1995). On a macro ANF scale, this results in the ANF becoming less stochastic or more deterministic (increased DPF gradient) as the diameter increases as found by Verveen (1962).

Returning to the types of conductance based stochastic models, the literature review by Goldwyn and Shea-Brown (2011) identified three types, all with the objective to approximate Markov chain models of channel noise. The first type of model identified is *sub-unit noise* in which a Gaussian noise term is added to the equations describing the fractions of open sub-units, i.e. the *m*, *n* and *h* HH differential equations. The second type of model identified is *conductance noise* which adds a Gaussian process directly into the fraction of open sodium channels, the m^3h term. However, it quickly becomes evident from literature that these two types of noise models are almost exclusively used in single node models due to their high computational requirements (Dangerfield et al. 2012; Huang et al. 2013; Mino et al. 2002; Rubinstein 1995). Consequently this makes these two types a non-viable option for practical implementation in compound ANF models used in the study of CIs for not only does each fibre have multiple nodes, but the compound model has multiple fibres spread along the length of the cochlea (Briaire and Frijns 2005; Kalkman et al. 2014; Malherbe et al. 2013; Malherbe et al. 2015).

The third and simplest type, *current noise*, adds a Gaussian noise current term to the HH $\delta V/\delta t$ equation which has the advantage of easy implementation and relatively low computational requirements (Jönsson 2010; Rattay et al. 2001b). Current noise is however shown to have two distinct deficiencies (Goldwyn and Shea-Brown 2011). The first deficiency is independence of the membrane voltage even though the noise intensity has been shown to be voltage dependent (Verveen and Derksen 1968). For the purposes of this study, noise intensity is regarded as a measure of the magnitude of the membrane noise amplitude of which the standard deviation is the rms noise. The second deficiency is the method's inability to inherently determine the noise intensity required to produce in vivo measured DPF spread (Rattay et al. 2001a; Shepherd and Javel 1997). At present the noise intensity has to be empirically calibrated as done by Jönsson (2010) by comparing the resulting discharge probability function's spread to measured data or by comparing the modelled noise intensity to measured noise intensity as in Rattay et al. (2001b).

This study presents a solution to both deficiencies through an alternative noise current term and novel voltage dependent current noise algorithm for application in conductance based ANF models used in CI modelling. Section two of the paper discusses the models and methods used in developing the new noise current model and the evaluation criteria used to validate the model. Section three validates the model output results as applied on a cat ANF model against that of measured cat ANF data and refines the model based on the results. Final remarks on the validity, application and possible deficiencies of the model, in particular for the human ANF, are discussed in section four.

2. Models and Methods

2.1. Auditory nerve fibre conduction model, morphology and stimulation

Because measured DPFs for human ANFs are not available, the proposed algorithm was developed using the cat ANF and in particular the HH-based compartmental cat ANF model with the morphology as presented in Rattay et al. (2001b) and reproduced in Fig. 1. However, for latter verification of the proposed algorithm against measured results, the ANF's diameters were adjusted based on the measured cat morphology by Rattay et al. (2013). The myelinated somatic diameter was decreased and kept constant at 16 μm while the central axon diameter was varied between the weighted values of $\mu \pm \sigma = 1.81 \pm 0.19$ μm to take into account the effect of varying nodal surface

areas in validating the algorithm. Using the ratio of fibre diameter (including myelin) over axon diameter (excluding myelin) of D/d = 1.43 in accordance with Rattay et al. (2013), the axon diameters correlate well with the weighted average fibre diameter of $\mu \pm \sigma = 2.62 \pm 0.44$ µm measured by Shepherd and Javel (1997). The measured diameters by Rattay et al. (2013) resulted in a variation in diameter of $d{\cdot}0.81 \leq d_{axon} \leq d{\cdot}1.0$ µm relative to Rattay's axon diameter $d = 2$ µm. For this particular study, simulated DPFs used to determine log(*RS*) vs log(d_{axon}) distributions were obtained for five specific axon diameter factors of DF_{axon} = (0.81, 0.86, 0.905, 0.95, 1.0) thereby including the measured $\mu = 1.81$ µm at $DF = 0.905$ and $\mu \pm \sigma$ diameters at $DF = 0.81$ and 1.0. In like manner the peripheral axon or dendrite diameter was varied between $\mu \pm \sigma = 1.02 \pm 0.12$ µm using DF_{dend} = (0.90, 0.96, 1.02, 1.08, 1.14) relative to the original dendritic diameter of 1 µm. If the k^{th} DF_{axon} value was used to set the axon diameter, the k^{th} DF_{dend} value was used to set the dendrite diameter. Nodal and compartmental lengths were kept unchanged and constant.

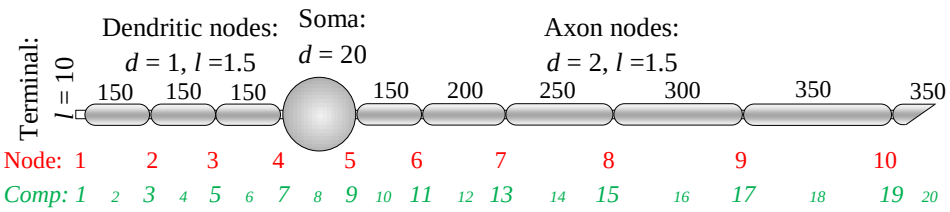

Fig. 1 A representation of a cat ANF giving all diameter (*d*) and length (*l*) values in µm as well as active node and compartment (Comp) numbers used in the paper. The fibre has in total thirty nine compartments of which twenty are active nodes and dimensions are as in Rattay et al. (2001b)

A bi-phasic, cathodic first stimulation with a 100 µs pulse width using a single monopolar point electrode in an infinite homogeneous medium (ρ_e = 0.3 kΩ·cm) was applied at a model temperature of 38°C (Bruce et al. 1999b; Rubinstein 1995; Shepherd and Javel 1997). The electrode was positioned 99 µm above node 2 of the straight ANF with $d_{axon} = 1.81$ µm and $d_{dend} = 1.02$ µm to obtain a deterministic threshold of 60 dB (re 1 µA) which is within the range of stochastic thresholds measured by Shepherd and Javel (1997). Final simulation results presented also used the curved cat fibre and spherical electrode as presented in Rattay et al. (2001b). All simulations were done in MATLAB using a first order implicit Euler-Maruyama numerical method based on Itô-calculus to solve the stochastic differential equations resulting from the introduction of the current noise terms. A time step-size of 1 µs was used in the numerical solver along with noise values that correspondingly changed every 1 µs (compared to the 2.5 µs in Rattay et al. (2001b)).

2.2. Validation of the current noise algorithm

To validate the proposed current noise model as an acceptable representation of an actual stochastic ANF, the simulated results were evaluated based on four criteria identified from literature:

i. The rms of the membrane noise (V_{rms}) vs transmembrane voltage (V_{mem}) must be an exponential function (Verveen and Derksen 1968).
ii. The spread of the modelled DPFs must be comparable to measured results. The measured DPFs for fibres BT-5-6, BT-5-14 and BT-5-19 in Shepherd and Javel (1997) were used having spreads of σ = 0.41, 0.77 and 1.18 dB respectively ($\bar{\sigma} = 0.79$).

iii. For an increase in diameter, the log(*RS*) vs log(*diameter*) must have a negative linear distribution (Rubinstein 1995; Verveen 1962). The axon diameter was used for validation and is calculated as $d_{axon} = 2 \times DF_{axon}$ µm

iv. The response latency must decrease for an increase in stimulus intensity (Rattay et al. 2001b; Shepherd and Javel 1997)

Obtaining discharge probability functions, RS and latency

Unless stated otherwise, the presented DPFs for specific *DF* values are the least square fit to fifteen discharge probabilities corresponding to fifteen stimulus levels (15 sets). The dB-range of the stimulus levels were chosen so as to limit the number of probabilities equal to 0 or 1 in order to provide a more accurate DPF fit. The discharge probability at a specific stimulus level (set) was calculated as the number of discharges out of a hundred iterations. The relative spread *RS* was then calculated as the standard deviation or spread of the DPF divided by the mean thereof. Latency was calculated as the time between the onset of the stimulus and the first action potential peak on any of the fibre nodes for each of the hundred iterations of each set.

2.3. An alternative expression for current noise

Figure 2 depicts the implementation of current noise in a section of a nerve fibre. Only a brief explanation of parameters and principles required for this paper will be presented here. For a detailed explanation of the methodology and calculation of the various components and voltages the reader is referred to Rattay et al. (2001b) and Rattay (1990).

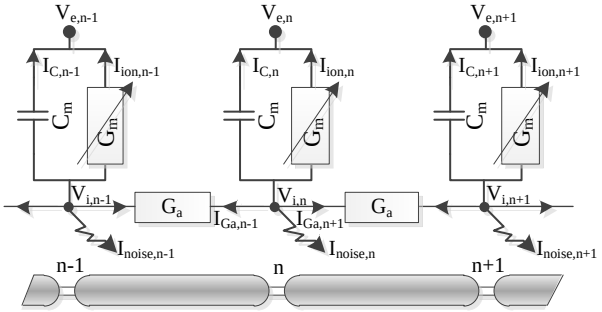

Fig. 2 A section of an ANF axon with three nodes (*n*) of Ranvier and internodal compartments with its corresponding standard electrical cable network. Electrical components shown are the axoplasmic conductance G_a, membrane capacitance C_m and voltage dependent membrane conductance G_m. V_i and V_e respectively represents the intra- and extracellular potentials. Currents indicated are the membrane capacitance current I_C, the potassium, sodium and leakage HH ionic currents represented by I_{ion}, the axoplasmic currents I_G and the injected noise current I_{noise}

An expression for the membrane capacitance current, $I_{C,n}$, is obtained via Kirchoff's current law at node *n* as:

$$I_{C,n} = C_m \frac{\delta V_{mem,n}}{\delta t} = -\left(I_{ion,n} + I_{noise,n}\right) + I_{st,n} \tag{1}$$

where $I_{ion,n}$ represents the ionic currents as defined by HH, $I_{st,n}$ represents the axoplasmic currents $\left(-I_{Ga,n-1} - I_{Ga,n+1}\right)$ and $I_{noise,n}$ the added Gaussian noise current. $V_{mem,n}$ is the transmembrane voltage at node *n* which can be expressed as:

$$V_{mem,n} = V_{i,n} - V_{e,n} = V_n + V_{rest} \tag{2}$$

where V_i and V_e respectively represents the intra- and extracellular potentials and the node voltage V_n is the deviation of $V_{mem,n}$ from the constant resting potential V_{rest}.

From these expressions it is evident that membrane voltage noise on a node is caused by the magnitude of the current noise affecting the rate of change of the membrane voltage. Equation (1) also shows that the effect of I_{noise} decreases as I_{ion} increases thereby effectively decreasing the membrane noise as seen and discussed in Rattay et al. (2001b), an effect that will henceforth be referred to as the inherent noise reduction characteristic.

The general term for the noise current for compartment *n* in Eq. (1) is expressed in Rattay et al. (2001b) as:

$$I_{\text{noise},n} = \text{GAUSS} \cdot k_{\text{noise}} \sqrt{A_n g_{\text{Na}}} \tag{3}$$

where k_{noise} (μA·mS$^{-0.5}$) is a common noise factor and GAUSS is a Gaussian term (μ = 0, σ = 1) of which the value changes every 2.5 μs. Since the standard deviation σ, or rms, of GAUSS is one, it implies that $I_{\text{rms,n}} = k_{\text{noise}} \sqrt{A_n g_{\text{Na}}}$ thereby suggesting that $RS \propto 1/I_{rms}$ as it has already been explained that $RS \propto 1/\sqrt{A \cdot g_{Na}}$. However, DPF simulation results shown in Fig. 3 for the original cat ANF noise model and temperature in Rattay et al. (2001b) with an increasing k_{noise}, ie I_{rms}, and a constant A_n show that $RS \propto k_{noise}$ and that therefore $RS \propto I_{rms}$.

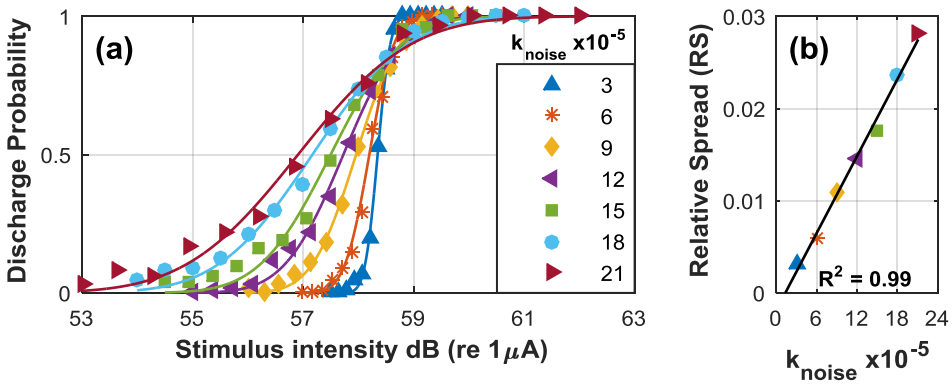

Fig. 3 (a) DPFs showing a decrease in gradient (increase in spread) with increasing k_{noise} values or equivalently proportional increasing relative spread as illustrated in **(b)** thus showing that $\boldsymbol{RS \propto k_{noise}}$ and hence $\boldsymbol{RS \propto I_{rms}}$. The electrode was positioned 114 μm above node 1 of the original cat model of **Error! Reference source not found.** at T = 28.9 °C

A more appropriate expression for current noise is therefore suggested as

$$I_{noise,n} = GAUSS \cdot k_{fact} \cdot 10^{-8} / \sqrt{A_n \cdot g_{Na}} \tag{4}$$

having a new noise factor k_{fact} (μA·mS$^{0.5}$) with the factor 10^{-8} included so as to have $k_{fact} > 1$ in simulations. This term correlates with the thermal noise equation (Horton 1987) in which $V_{rms} \propto \sqrt{R}$ and since resistance (R) is inversely proportional to area, it can be stated that $V_{rms} \propto 1/\sqrt{A}$.

The introduction of this alternative current noise term added an additional noise reduction factor to the inherent noise reduction in Eq. (1) in that I_{noise} now decreases with an increase in fibre diameter in contrast to I_{noise} increasing in the original noise current term. As will be shown in the results, this led to more deterministic DPFs, or equivalently lower *RS* values, for larger fibre diameters compared to the original term.

2.4. Creating a voltage dependent current noise

In order to obtain a voltage dependent current noise, so as to model the fluctuations of the voltage dependent sodium channels within the proposed algorithm, k_{fact} ultimately had to be made a function of the node voltage V_n defined in Eq. (2). A simplified diagram of the proposed algorithm to be discussed in this section is shown in Fig. 4.

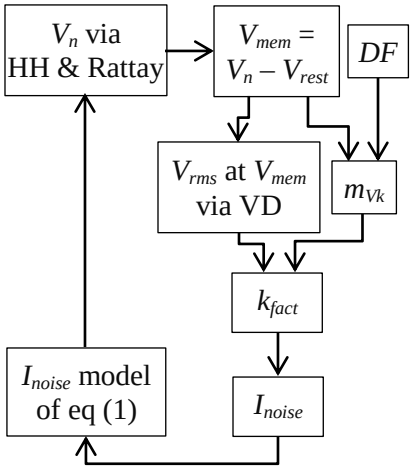

Fig. 4 Simplified diagram of the proposed voltage dependent current noise algorithm. HH = Hodgkin & Huxley, *DF* = Diameter Factor, VD = Verveen & Derksen, m_{Vk} = noise gradient function

First the HH-based compartmental model in Rattay et al. (2001b) is solved to obtain V_n from which the transmembrane voltage $V_{mem,n}$ is calculated using Eq. (2). From $V_{mem,n}$ the required rms noise voltage (V_{rms}) on the node is calculated via a least square function fitted to the measured data in Verveen and Derksen (1968) (VD) as shown in Eq. (5) and Fig. 5.

$$V_{rms} = 0.549e^{0.0137 \cdot V_{mem}} \tag{5}$$

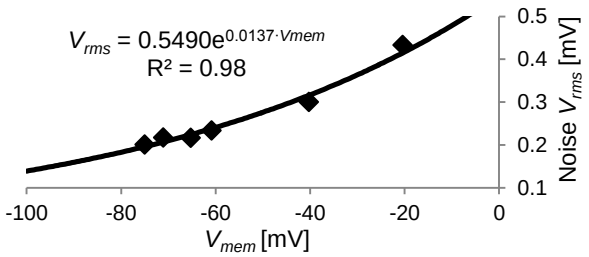

Fig. 5 Reproduction of the measured data by Verveen and Derksen (1968) depicting the rms membrane noise voltage (V_{rms}) versus the transmembrane voltage (V_{mem}) for the myelinated axons of a frog sciatic nerve at room temperature with a least square exponential function fit

Since the origin of the membrane noise is the voltage fluctuations of the sodium channels of which the number is determined by the area of the node, the calculated V_{rms} can however only serve as a reference. This is because the VD measurements were on myelinated axons of a frog's sciatic nerve of which the Ranvier node diameters were kept in the order of 4 μm, but the nodal lengths varied between 0.5 and 1.0 μm. The reference voltage V_{rms0}, at the VD's reference nodal surface area A_0, therefore had to be scaled to $V_{rms,n}$ at the actual membrane surface area of compartment n, A_n, of the cat ANF. For the purposes of this study A_0 was calculated as a cylindrical area assuming an average nodal length of 0.75 μm: $A_0 = 4 \times 0.75 \times \pi = 3\pi$ μm^2.

Based on the origin of the noise it followed that scaling V_{rms0} to $V_{rms,n}$ should be based on a relationship between A_0 and A_n. Having shown that $I_{rms} \propto 1/\sqrt{A \cdot g_{Na}}$, a relationship between V_{rms}

and A was determined by first finding the relationship between V_{rms} and I_{rms} or k_{fact} which is shown in Fig. 6a to be linear. It can therefore be stated that $V_{rms} \propto I_{rms} \propto RS \propto 1/\sqrt{A}$ and scaling V_{rms0} to $V_{rms,n}$ can thus be partially done using Eq. (6):

$$V_{rms,n} = V_{rms0} \times \frac{\sqrt{A_0}}{\sqrt{A_n}}\, mV \tag{6}$$

Fig. 6a also provided the key for achieving the original objective of determining k_{fact} as a function of V_n in order to obtain a voltage dependent current noise by writing from Fig. 6a the expression:

$$k_{fact,n} = \frac{V_{rms,n}}{m_{Vk,n}} \tag{7}$$

Therefore, if the gradient m_{Vk} is known along with the required V_{rms}, obtained via the VD function, the k_{fact} value required to generate the required V_{rms} can be calculated. It is however evident from the difference in gradients in Fig. 6a that V_{rms} and hence m_{Vk} is also a function of the nodal diameter ($d_{axon} \approx 1.8 \cdot d_{dendrite}$). Hence k_{fact} not only became a function of V_n, but also of the diameter factor DF via the gradient m_{Vk} as shown in Fig. 4.

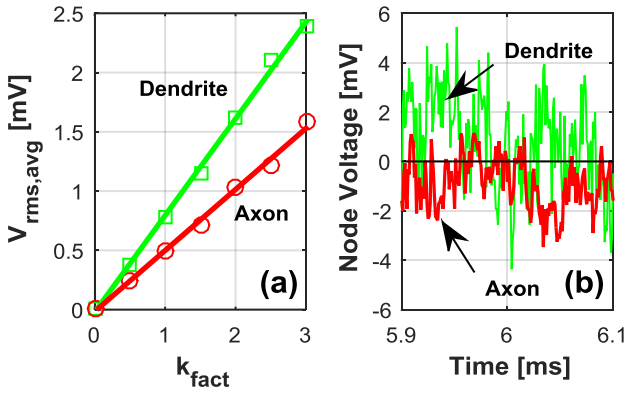

Fig. 6 (a) V_{rms} vs k_{fact} for the axon and dendrite shows a distinct linear relationship. V_{rms} was calculated as the average standard deviation of the voltages on nodes 2 and 3 of the dendrite and nodes 8 to 19 of the axon for the cat ANF at various k_{fact} values. (b) An example of the voltage noise showing the node voltage V_n for nodes 3 (dendrite) and 14 (axon) at k_{fact} = 3 and without noise at k_{fact} = 0 (zero line). Note the higher dendritic V_{rms} values compared to the axon's for the same k_{fact} value in both figures due to the dendrite's smaller nodal membrane surface area. Simulations were done with no external stimulus (resting state)

Finally, in order to compensate for the inherent noise reduction characteristic of a current noise model within the proposed algorithm, m_{Vk} is shown in Fig. 4 to have been made a function of V_n via V_{mem} as well. The procedure followed to determine m_{Vk} as a function of V_n is explained in detail in the next section.

2.5. Gradient m_{Vk} as a function of DF and V_{mem}

Summarised below are the steps taken to determine the gradient m_{Vk} as a function of the diameter factor DF and transmembrane voltage V_{mem}. Though all figures shown are for the dendrite, the same process was also followed for the axon so as to obtain an equivalent axon gradient function.

i. Extract the noise from the stochastic APs and calculate V_{rms} vs V_{mem} for the active nodes for k_{fact} = (0.5, 1.8, 3.1, 4.4, 5.7, 7.0) for each DF_{dend} = (0.90, 0.95, 1.00, 1.05, 1.10, 1.15). The

values for k_{fact} were chosen based on preliminary simulations as to which values provide noise within the range measured by VD and the *DF* values so as to include the range of measured diameter values. For the axon DF_{axon} = (0.80, 0.85, 0.90, 0.95, 1.00, 1.05) was used.

ii. Do a linear regression for V_{rms} vs V_{mem} for each k_{fact} and *DF* as shown in Fig. 7a (for *DF* = 0.95) to obtain m_1 and c_1 from $V_{rms} = m_1 \cdot V_{mem} + c_1$. The negative gradients are a realisation of the inherent noise reduction characteristic of the current noise model in Eq. (1).

iii. Calculate $V_{rms} = m_1 \cdot V_{mem} + c_1$ for V_{mem} = (-90, -80, …, +30, +40) mV at each k_{fact} for all *DF* values. For each *DF*, plot V_{rms} vs k_{fact} for each V_{mem} and then do a linear regression for V_{rms} vs k_{fact} as illustrated in Fig. 7b (for *DF* = 0.95) in order to obtain m_{Vk} and c_{Vk} from $V_{rms} = m_{Vk} \cdot k_{fact} + c_{Vk}$. For example, if a vertical line is drawn in (a) at V_{mem} = 0, the six intersections with the six k_{fact} lines are represented as six markers in (b) forming a linear line for V_{mem} = 0 of which the gradient is m_{Vk}. Observe the direct proportionality of V_{rms} vs k_{fact} as already noted in Fig. 6a and that, though not shown, all the regression lines approximately converges at the origin resulting in $c_{Vk} \approx 0$.

iv. For each *DF* value, plot the gradient m_{Vk} of each line in Fig. 7b versus its corresponding V_{mem} value and do a linear regression as shown in Fig. 7c to find the required gradient m_{Vk} as a function of V_{mem} for each *DF*. Each marker in (c) therefore represents the gradient of a line for a specific *DF* and V_{mem} value in (b). Each line in (c) would have its own set of corresponding curves shown in (a) and (b).

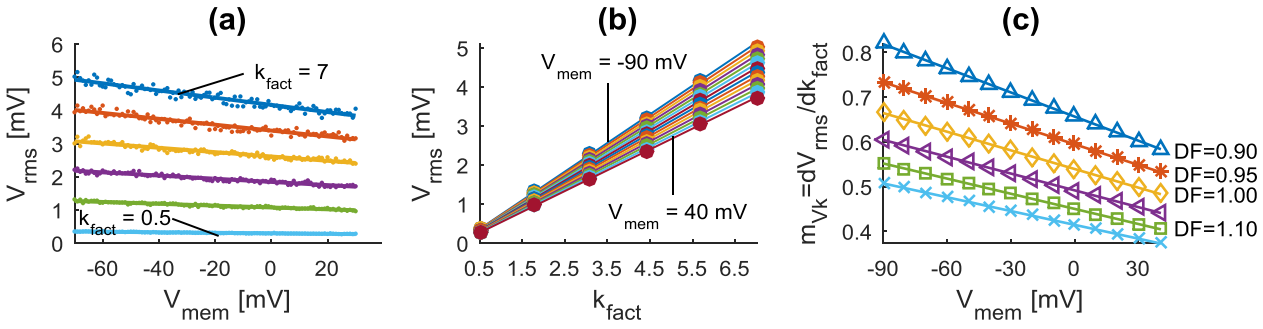

Fig. 7 (a) Linear regression of simulated V_{rms} vs V_{mem} data for *DF* = 0.95 starting at k_{fact} = 7 at the top through to k_{fact} = 0.5 at the bottom in decrements of 1.3. Each set of markers for a k_{fact} value is the result of 100 iterations of the straight cat ANF model. Note the negative gradient due to the inherent noise reduction characteristic in Eq. (1). **(b)** Linear regression of V_{rms}, calculated based on the linear regression in (a), versus k_{fact} for V_{mem} = -90mV at the top through to V_{mem} = 40 mV at the bottom in 10 mV increments – a line for each V_{mem} value. Each set of six markers for a specific V_{mem} is the intersection points of a vertical line at the specific V_{mem} value with the six regression lines for *DF* = 0.95 in (a). **(c)** The gradient of each regression line in (b) plotted against the line's V_{mem} value for each *DF*. Each marker thus represents the gradient of the linear regression in (b) for a specific V_{mem} and *DF* value

v. Finally m_{Vk} as a function of V_{mem} for any value of *DF* can now be found using interpolation. This is illustrated in Fig. 8 showing a 3D mesh rendering of Fig. 7c with the cubic spline interpolated m_{Vk} gradient function for the dendrite at DF_{dend} = 0.975 in (a) and for the axon at DF_{axon} = 0.875 in (b).

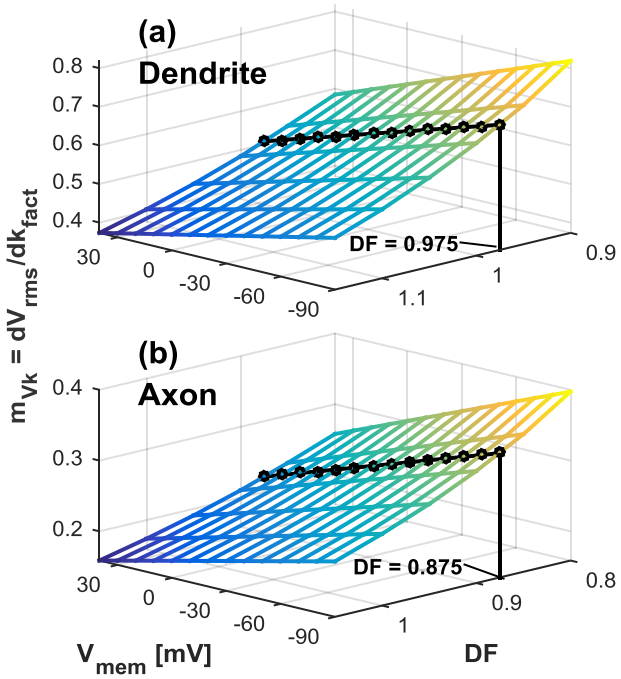

Fig. 8 3D Mesh rendering of Fig. 7c showing the interpolated gradient function for the dendrite at DF_{dend} = 0.975 in (a) and for the axon at DF_{axon} = 0.875 in (b)

3. Results

3.1. Evaluation of the proposed expression for current noise

Application of only the proposed voltage independent current noise term in Eq. (4) to the straight cat ANF model at DF_{dend} = 1.02, DF_{axon} = 0.905 and T = 38°C required a manually calibrated k_{fact} = 3.5 to approximate the average measured spread of σ = 0.79. The resulting DPF with σ = 0.81 is shown in Fig. 9a along with the DPFs for the remaining four *DF* values. The DPF spreads monotonically decrease with increasing *DF* and consequently the resulting log(*RS*) vs log(d_{axon}) (log-log) distribution in (b) has the negative linear distribution as required by validation criterion iii.

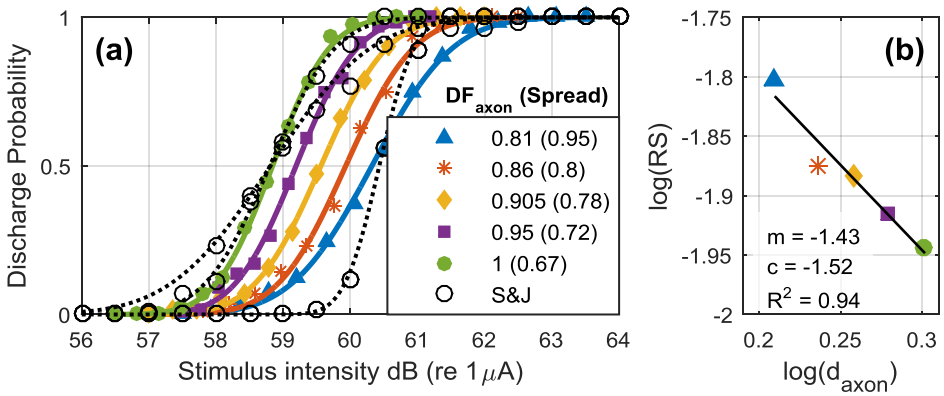

Fig. 9 (a) Average of three simulations' DPFs of the straight cat ANF for DF_{axon} = (0.81, 0.86, 0.905, 0.95, 1.0) with application of only the proposed current noise expression in Eq. (4) (constant k_{fact} = 3.5) compared to the measured data of Shepherd and Javel (1997) (Broken lines). This constitutes a voltage independent current noise with no inherent noise reduction compensation. The DPFs show a monotonic decrease in spread from with increasing *DF* and consequently the log(*RS*) vs log(d_{axon}) distribution in **(b)** has the required negative linear distribution

In contrast, Fig. 10 shows that the application of the original current noise term in Eq. (3) with k_{noise} = 40×10^{-5} does not result in a monotonic decreasing DPF spread and consequently not a negative linear regression for the log-log distribution either. It is true that the original term in Eq. (3) sees a reduction in noise upon an increase in diameter even though $I_{noise} \propto \sqrt{A_n}$. However, this is because I_{noise} is added to I_{ion} in Eq. (1), and as Rattay et al. (2001b) mentioned, $I_{ion} \propto A_n$ and hence I_{ion} dominates I_{noise} at larger diameters making the effect of the noise relatively smaller and hence the noise decreases. This decrease in noise is however not sufficient to result in the required negative linear log-log distribution.

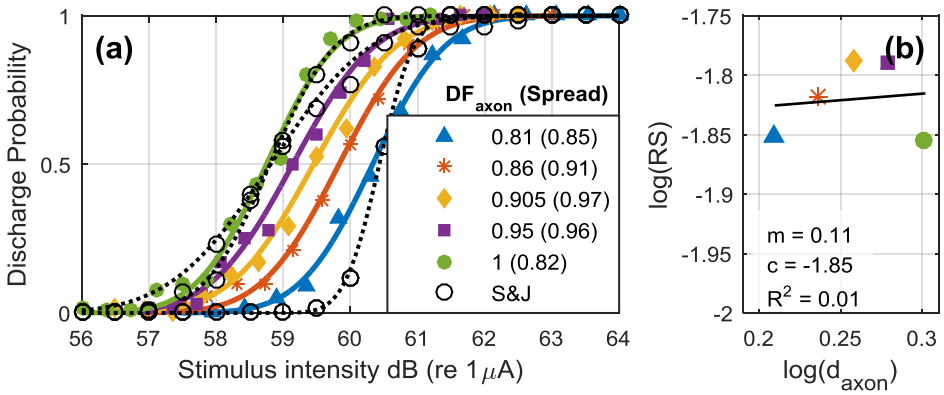

Fig. 10 (a) Application of the original Rattay current noise term in Eq. (3) with a constant k_{noise} = 40×10^{-5} on the straight cat ANF for DF_{axon} = (0.81, 0.86, 0.905, 0.95, 1.0) resulted in non-monotonic DPF spreads and consequently the log-log distribution in **(b)** does not have the required negative linear distribution

The proposed current noise term in Eq. (4) is therefore indeed a more appropriate term to use when compared to measured DPFs. But since both current noise terms are independent of V_{mem} and both have the inherent noise reduction characteristic, neither adheres to the first validation criterion of an exponential V_{rms} vs V_{mem} without incorporating the current noise term into the proposed voltage dependent current noise algorithm.

3.2. Evaluation of V_{rms} vs V_{mem} for the proposed current noise algorithm

To determine the adherence of the voltage dependent current noise algorithm in Fig. 4 to the first validation criterion, the algorithm was applied to the straight cat ANF model at DF_{axon} = 0.81 and DF_{dend} = 0.90 from which V_{rms} vs V_{mem} was estimated. The result in Fig. 11 shows a near perfect correlation between the modelled data scaled to A_0 (solid markers) and the measured exponential VD function for both the dendrite and the axon. Thus the first model validation criterion, an exponential V_{rms} vs V_{mem} distribution, is satisfied. Also shown is the unscaled V_{rms} values (empty markers) for the dendrite which are higher than that of the axon's as would be expected due to dendrite's smaller diameter and hence nodal diameter A_n resulting in a higher I_{noise} and thus V_{rms}.

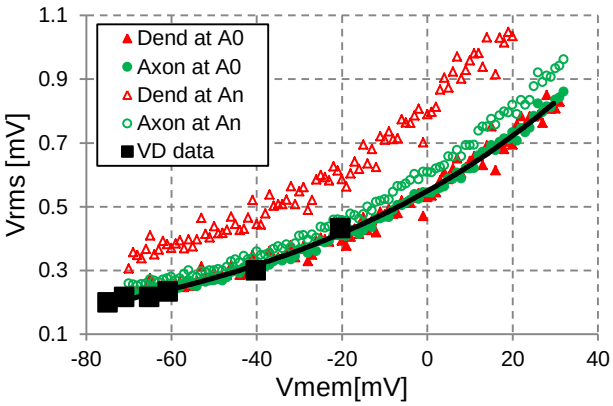

Fig. 11 The proposed algorithm provides a near perfect correlation for an exponential V_{rms} vs V_{mem} for both the dendrite and axon when compared to the measured VD data and scaled to A_0 (solid markers). If left unscaled (empty markers), it can be seen that the dendrite's noise is higher than the axon's as expected due to the dendrites smaller diameter and hence smaller nodal surface area

3.3. Comparison between modelled and measured spread

The second validation criterion requires the spread of the modelled DPF to correlate with measured DPFs. Fig. 12 however shows the modelled cat ANF at the average diameters (DF_{dend} = 1.02, DF_{axon} = 0.905) to have a spread of σ = 0.15 which is significantly lower than those measured by Shepherd and Javel (1997) (σ = 0.41, 0.77, 1.18) thereby suggesting a too small a noise current. To compensate for the difference in spread a scaling factor (*SF*) was thus included into Eq. (4) as shown in Eq. (8) in order to increase the noise current and hence the spread.

$$I_{noise,n} = GAUSS \cdot \frac{k_{fact,n} \cdot 10^{-8}}{\sqrt{A_n \cdot g_{Na}}} \times SF \tag{8}$$

After simulation at a number of *SF* values, Fig. 12 shows that an *SF* = 4.9 would sufficiently approximate the average measured spread (σ = 0.79) at the average measured diameters.

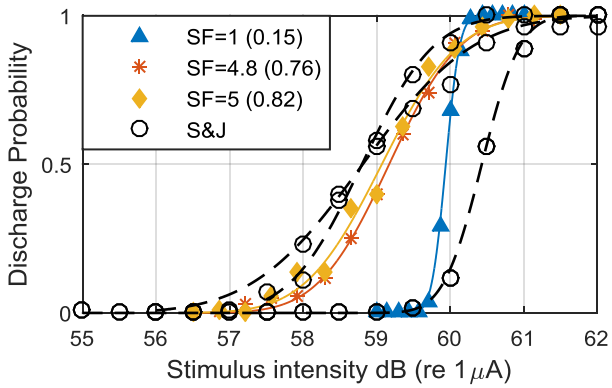

Fig. 12 Least square fitted DPFs of the straight cat ANF current noise model for scaling factors *SF* =1, 4.8 and 5 and associated standard deviations (spreads) in brackets. At SF = 1 the modelled spread (0.15) is much lower than the measured data of Shepherd and Javel (1997) having σ = 0.41, 0.77 and 1.18. From the results at *SF* = 4.8 and 5.0 an *SF* = 4.9 would sufficiently approximate the average measured spread of 0.79. The stimulus electrode was positioned 0.99 mm above node 2, DF_{dend} = 1.02, DF_{axon} = 0.905, T = 38°C

3.4. *Log-Log test of the algorithm with the scaling factor*

Including the constant *SF* = 4.9 into the proposed current noise algorithm did however not result in adherence to the third validation criterion. The five modelled DPF spreads in Fig. 13a do not consistently decrease with increasing *DF* and consequently the resulting log(*RS*) vs log(d_{axon}) distribution in (b) does not have a significant negative linear distribution.

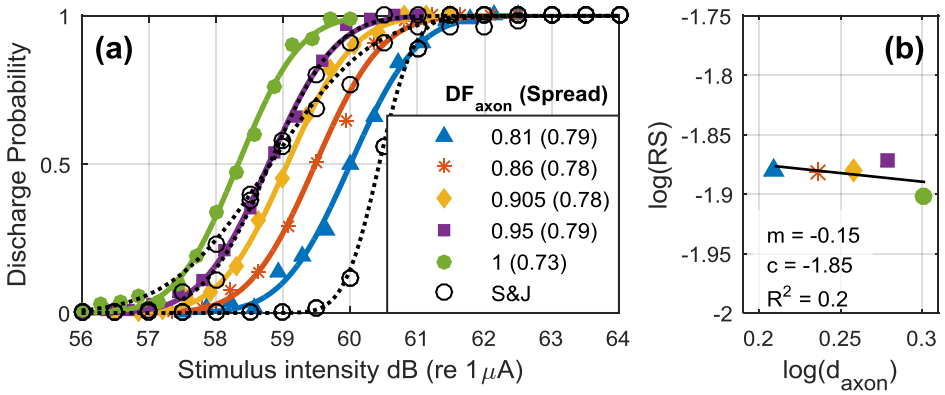

Fig. 13 (a) DPFs of the straight cat ANF using the proposed current noise algorithm with *SF* = 4.9 for all *DF* values. The DPFs do not show a monotonic decrease in spread with increasing *DF* and consequently the log-log distribution in **(b)** does not have a significant negative linear distribution

The reason becomes apparent when noting that while the required $V_{rms,n}$ decreases as *DF* increases through Eq. (6), the required gradient m_{Vk} simultaneously also decreases (Fig. 7c) with the net result that $k_{fact,n}$ in Eq. (7) increases as *DF* increases. Hence compensating for the inherent noise reduction characteristic in order to adhere to the measured exponential V_{rms} vs V_{mem} criterion comes at the cost of non-adherence to the negative linear log-log relationship criterion. If however *SF* can be made a function of the diameter or *DF* such that *SF* decreases with increasing diameter, the spread can be reduced as the diameter increases.

3.5. *Noise scaling factor as a function of the diameter factor*

From Fig. 13 we noted that the application of the proposed algorithm in Fig. 4 resulted in a log-log gradient of almost zero whereas the use of only the proposed current noise term in Eq. (4) resulted in the desired negative linear log-log distribution in Fig 9. From the simulation results in Fig. 3 it was also noted that $RS \propto k_{noise}$ and hence one would expect that $RS \propto SF$. This linear relationship is verified in Fig. 14 having used the same method as in Fig. 12 by excluding the proposed algorithm and using only the proposed current noise term at the average diameters (DF_{dend} = 1.02, DF_{axon} = 0.905) to determine *RS* at *SF* = (1, 2, 3, 4, 5, 5.5).

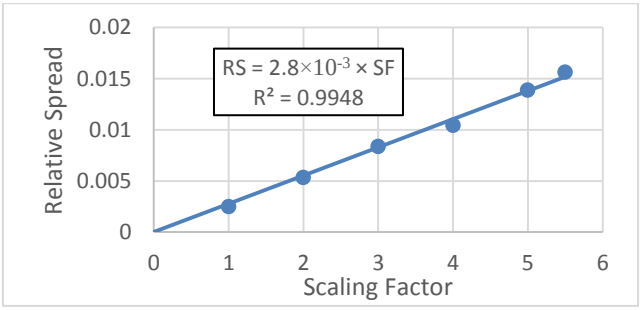

Fig. 14 *RS* as a function of *SF* when the ANF is modelled using only the proposed current noise term in Eq. (4). The result is a near perfect least square linear fit confirming as expected that *RS* is directly proportional to *SF* when using the proposed current noise term.

Knowing that we need to obtain a negative linear log-log gradient, we can write *RS* as a function of the axon diameter from which, based on the result in Fig. 14, we can write the required *SF* as a function of d_{axon} in Eq. (9):

$$\begin{aligned} \log RS &= m \log d_{axon} + c \\ RS &= 10^{m \log d_{axon} + c} \\ 0.0028 \cdot SF &= 10^{m \log d_{axon} + c} \\ SF &= 357 \times 10^{(m \log d_{axon} + c)} \end{aligned} \tag{9}$$

Substituting the gradient of m = -1.43 and intercept of c = -1.52 found in Fig. 4b into Eq. (9), the estimated *SF*'s required to provide a negative linear log-log distribution values at the five DF_{axon} values are calculated and plotted in Fig. 15. The result is a power function for *SF* vs DF_{axon}/DF_{avg} in the form of Eq. (10) in which the exponent (-1.43) is the gradient *m* and the coefficient (4.68), which proved to be an exponential function of the absolute value of the intercept *c*, is nearly equal to the initial scaling factor of *SF* = 4.9 determined in Fig. 12. Equation (10), in which SF_{DF} is the scaling factor to be used for the specific diameter factor DF_{axon} and DF_{avg} = 0.905, thus provides a way in which to control the gradient of the log-log distribution primarily through the exponent, and the intercept of the log-log distribution primarily through the coefficient. Both the exponent and coefficient affects the DPF spreads.

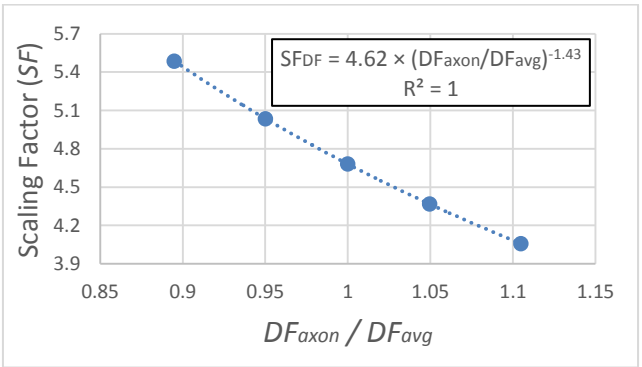

Fig. 15 A perfect power function fit of the calculated *SF*s required to produce a linear log-log distribution versus DF_{axon}/DF_{avg} at the five DF_{axon} values. The exponent of the function primarily controls the gradient of the log-log distribution whilst the coefficient primarily affects the intercept thereof.

$$SF_{DF} = 4.62 \times \left(\frac{DF_{axon}}{DF_{avg}}\right)^{-1.43} \tag{10}$$

Figure 16 shows the result of replacing the constant *SF* = 4.9 in Eq. (8) with the diameter dependent SF_{DF} in Eq. (10) within the proposed current noise algorithm. The DPFs shows a favourable monotonic decrease in spread with increasing diameter and consequently the required negative linear log-log distribution. The gradient of the log-log distribution is lower (steeper) compared to m = -1.43 in Fig. 9b when using only the proposed current noise term in Eq. (4). This can be seen in view of the fact that the proposed algorithm does not completely nullify the effect of the current noise term and hence Eq. (10) decreases the gradient relative to that of Fig. 9b.

Another observation worth noting is the small variance of the spreads which can directly be ascribed to the small variance of the axon diameters. Yet the algorithm is capable of producing the negative linear log-log distribution.

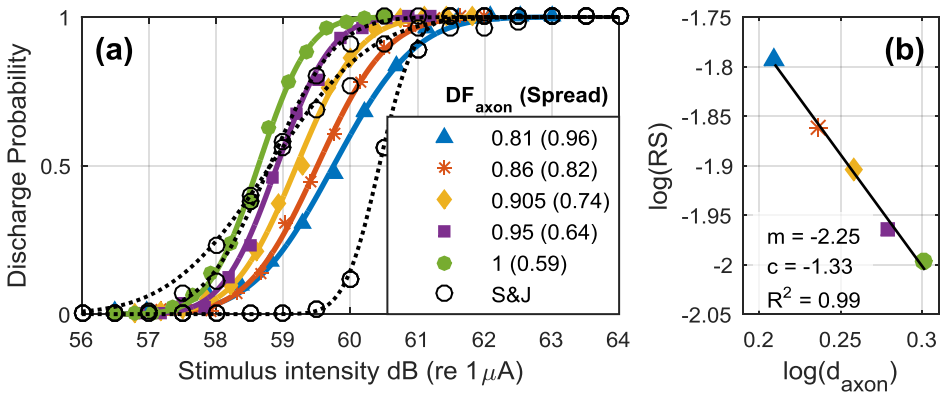

Fig. 16 Average result of three simulations of the straight cat ANF using the diameter dependent SF_{DF} in Eq. (10) within the proposed algorithm. The average DPFs in (a) show the required decreasing spread with increasing *DF* whilst the average log-log distributions in (b) show the required negative linear distribution.

3.6. Latency versus stimulus intensity test

The fourth and final validation criterion requires the response latency to decrease with an increase in stimulus intensity. The algorithm is shown to adhere to this criterion in Fig. 17 depicting the DPF and corresponding latency results for DF_{axon} = (0.81, 0.905, 1) for one of the simulations used in Fig. 16. Also worth noticing is the decrease in the latency variance with increasing fibre diameter due to the corresponding decrease in the noise V_{rms}.

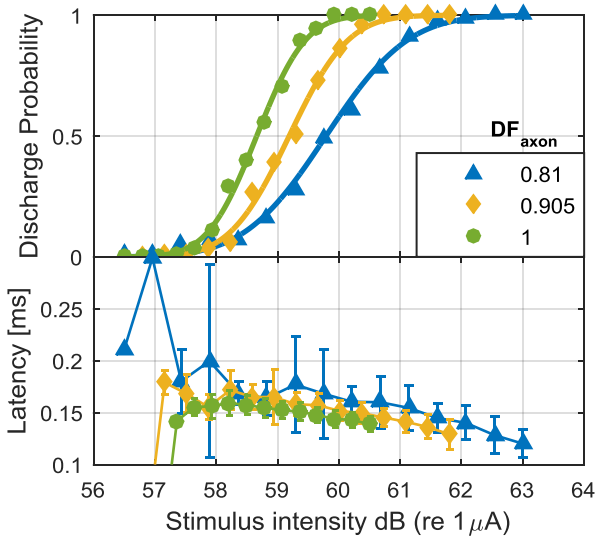

Fig. 17 (a) DPFs for DF_{axon} = (0.81, 0.905, 1.0) of a simulation in Fig. 16 along with their corresponding latency plots in (b) showing a steady decrease in latency with an increase in stimulus intensity as required. Noticeably the variance in latency also decreases with an increase in diameter due to the corresponding decrease in the noise V_{rms} . The large variance in latency for DF = 0.81 at approximately 58 dB is because of significant variance in the low number of latencies at the low stimulus (probability) levels.

3.7. Curved cat fibre implementation

A final evaluation of the proposed algorithm was made through application to the curved cat fibre in Rattay et al. (2001b) illustrated in Fig. 18a. Although the spreads of the DPFs in (b) do decrease monotonically and do result in the required negative linear log-log distribution in (c), the log-log gradient is significantly higher (less steep) than for the straight fibre in Fig. 16. However, when compared to the increasing DPF spreads and positive log-log gradient in Fig. 19 when using the original current noise term in Eq. (3) and when compared to Fig. 20 using only the proposed current noise term in Eq. (4), the proposed algorithm still provides the best and most sound biological results in terms of spread and log-log distribution.

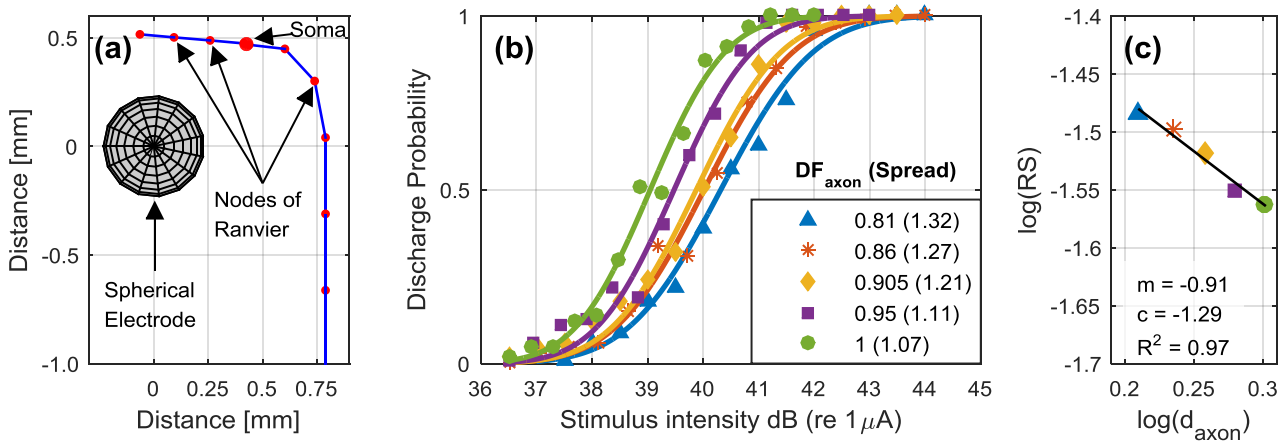

Fig. 18 (a) Curved cat ANF with a spherical electrode in a homogeneous conductive medium as in Rattay et al. (2001b). **(b)** DPFs of a single simulation show a monotonic decrease in spread with increasing diameter which results in the required negative linear log-log distribution in **(c)** albeit with a higher (less steep) gradient compared to the straight fibre.

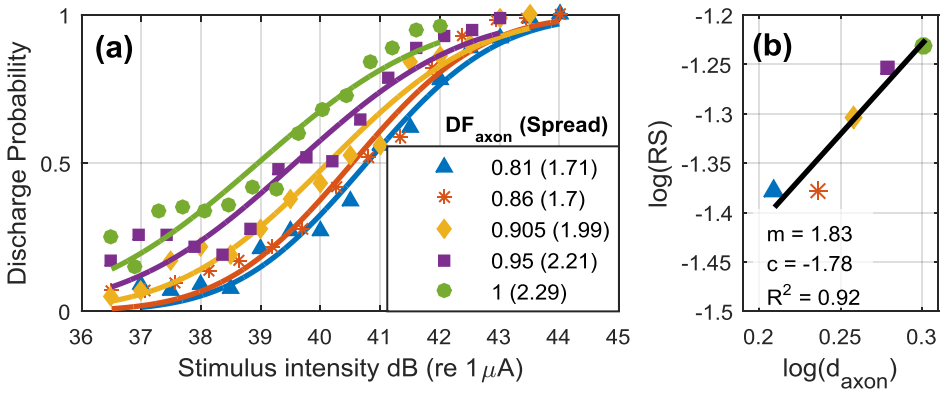

Fig. 19 Application of the original voltage independent current noise term in Eq. (3) (k_{noise} = 40×10^{-5}) to the curved cat fibre in Fig. 18 results in the DPFs in (a) having an increase in spread instead of the biologically measured decrease in spread with an increase in diameter and in a log-log distribution with a positive instead of negative linear distribution in (c)

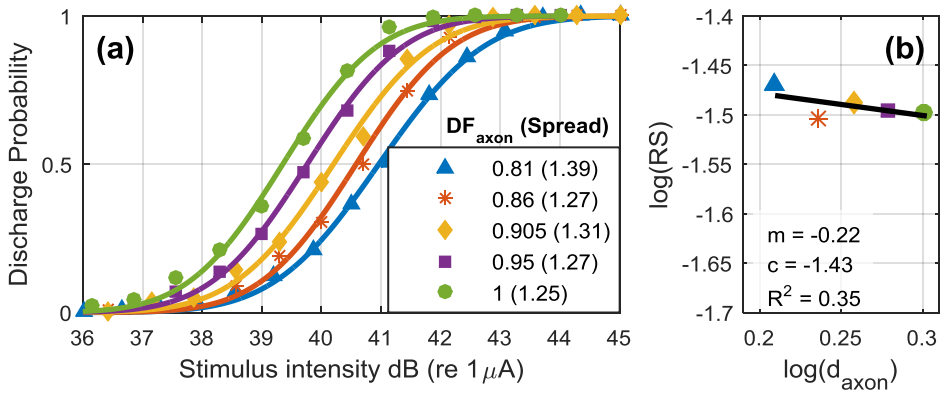

Fig. 20 Application of the proposed voltage independent current noise term in Eq. (4) (k_{fact} = 3.5) to the curved cat fibre in Fig. 18a results in the required negative linear log-log distribution in (b) despite the DPFs in (a) not having a monotonic decrease in spread with an increase in diameter. The results are averaged over five simulations.

Finally Fig. 21 verifies that the latencies decrease with an increase in stimulus intensity as biologically measured. The initial increase in latency at the lower probabilities can again be ascribed to a combination of the low number of discharges and the high variance in latency.

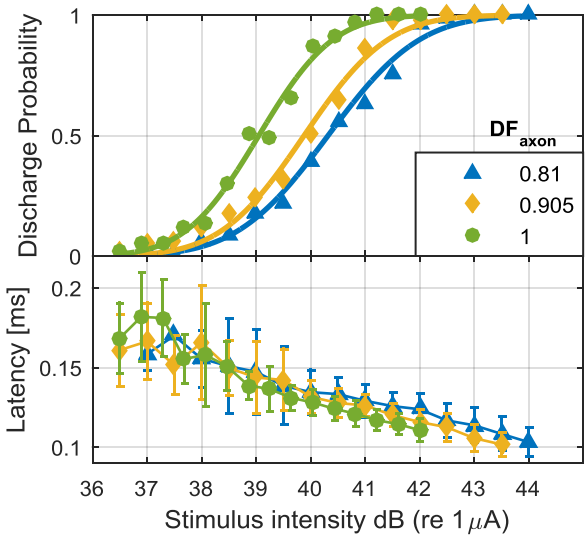

Fig 21 (a) DPFs for DF_{axon} = (0.81, 0.905, 1.0) in Fig. 18 show a steady decrease in latency with an increase in stimulus intensity as required. The initial increase in latency at the lower probabilities can be ascribed to a combination of the low number of discharges and the high variance in latency

4. Discussion and Conclusion

The contribution of this paper is twofold. Firstly a more appropriate current noise term was presented in Eq. (4) that provided the biological negative linear log(*RS*) vs log(*d*) distribution. However, the term remains independent from the source of the voltage noise, namely the transmembrane voltage. Consequently the magnitude of the current noise remains constant as dictated by an empirically calibrated k_{fact} which results in a negative linear V_{rms} vs V_{mem} relationship (Fig. 7a) instead of the biological exponential relationship (Fig. 5, Verveen and Derksen (1968)). The second contribution addressed this shortcoming through a voltage dependent current noise algorithm (Fig. 4) adhering to four identified validation criteria.

Including or excluding the voltage dependant algorithm into a model depends on the information and accuracy required from the model. If the modeller requires only the DPFs and log(*RS*) vs log(*d*) distributions to study the effect of varying diameters on discharge probability, only the proposed current term in Eq. (4) needs to be implemented. It was however noted in Fig. 20 that application of only the current noise term does not yield as good results in terms of the log-log gradient when compared to including the voltage dependent algorithm in Fig. 18. Hence, for improved results and in order to obtain the exponential V_{rms} vs V_{mem} distribution for possible further evaluation or as an input to other modelling algorithms, the voltage dependent algorithm has to be included.

Inclusion of the proposed algorithm also resulted in a 28% reduction in computational time compared to using only the proposed current noise term. This can be ascribed to the algorithm resulting in lower V_{rms} at low V_{mem} values enabling the numeric solver to converge faster to an answer within an acceptable error. The reduction in computational cost of the algorithm was calculated based on the computational time for 100 iterations each over a 600 μs simulation period at DF_{axon} = 0.905 and a stimulation resulting in discharge probability of one. The processor used was an Intel® Core™ i5-6200U CPU, at 2.30 GHz, 7.87 GB usable RAM on a 64 bit operating system. For the voltage *independent* method (k_{fact} = 3.5, I_{stim} = 63 dB) the computational time was

approximately 1050 seconds versus approximately 750 seconds for the proposed voltage *dependent* current noise algorithm (I_{stim} = 63 dB). The proposed algorithm thereby retains and even improves the low computational cost relative to the conductance and sub-unit types of conductance based stochastic models and even more so compared to Markov chain models. Computationally this makes the proposed algorithm the most suitable for application in compound ANF models used in CI modelling which will be the focus of a follow up paper.

Three matters remain regarding the model presented: the effect of temperature, the log(*RS*) vs log(*d*) gradient if applied to human ANFs and thirdly the fact that human ANFs have a long unmyelinated pre-somatic region and an unmyelinated soma which acts as active nodes within the model (Rattay et al. 2001b).

Considering first the unmyelinated pre-somatic region and soma of the human ANF, it has been noted before that an increase in diameter or surface area of an unmyelinated, active node will cause the node to become less stochastic or "noisy" as the significance of a single sodium channel decreases compared to the total ionic conductance (Bruce et al. 1999b; Rubinstein 1995). Both the proposed current noise term in Eq. (8) and the diameter dependent scaling factor in Eq. (10) ensure that the model decreases the noise on a node with increasing diameter to ensure the required negative linear log-log distribution. Hence, in the case of the human soma and pre-somatic region having significantly larger surface areas compared to the nodes of Ranvier, the proposed model will cause a reduction in noise on these active unmyelinated noise. In contrast, the original current noise term in Eq. (3) will increase instead of decrease the current noise on the soma and pre-somatic region as well as on the nodes of Ranvier which will then most probably result in a positive instead of negative linear log-log distribution in view of the results for the straight (Fig. 10) and curved (Fig. 19) CAT ANF models as well as the increase in *RS* vs k_{noise} in Fig. 3b. Keeping the overall objective of modelling the threshold variability of the ANF in mind, it is the noise on the nodes of Ranvier that will mostly affect the threshold variability of the human ANF as it is on these nodes that the noise magnitude are the greatest and where the APs are initiated.

Temperature might be a possible concern because the measurements in Verveen and Derksen (1968) which forms the reference for determining V_{rms0} were done at room temperature in contrast to the 38°C of Shepherd and Javel (1997). Because measured membrane noise (V_{rms}) vs temperature data could not be found in literature, it was considered to partially include the effect of temperature through a temperature dependent g_{Na} having a Q_{10} =1.02 (Smit et al. 2008). However, with g_{Na} = 635 ms/cm^2 at 20°C vs 658 ms/cm^2 at 38°C and the root of the ratio being 0.98, this made an insignificant difference to I_{noise} in Eq. (4). An alternative approach considered was to apply the thermal noise relationship to temperature in which $V_{rms} \propto \sqrt{T}$, but as Horton (1987) alludes, membrane noise is not thermal noise. In fact, Monte-Carlo simulations of a stochastic Markov version of the Mainen-Sejnowski model of dendritic excitability in cortical neurons showed a decrease in voltage noise with temperature due to membrane acting as a low-pass RC filter to the increasing bandwidth of the voltage noise as channel transition rates increase with temperature (Manwani et al. 1999).

The final matter pertains to the log-log gradient should the model be applied to human ANFs. Although the modelled log-log gradient for the cat ANF is a reasonable approximation because of the DPF spreads falling within the measured ranges by Shepherd and Javel (1997), equivalent in vivo ANF DPF measurements do not exist for human ANFs. As a consequence, even though the noise gradient functions can be determined for the human ANF as in Fig. 8, the value of the exponent and coefficient in Eq. (10) which determines the log-log gradient and intercept cannot be verified at this

time. Therefore the values used for the cat ANF will have to serve as initial estimates for the human ANF as well.

While keeping the matters discussed above in, the model provides a computationally feasible means of including non-phenomenological stochasticity into conductance based, compound ANF models used in CI modelling by providing an exponential membrane noise (V_{rms}) vs transmembrane voltage (V_{mem}), biologically comparable discharge probability functions and negative linear log(*RS*) vs log(*diameter*) distributions.

Appendix A

This section provides a step-by-step procedure on how to implement the proposed algorithm into existing current noise models. It also serves as an encapsulation of the algorithm in a chronological order of its application.

1. The first and most time consuming step is to determine the dendrite and axon noise gradient functions m_{Vk} as described in section 2.5 using the proposed current noise term in Eq. (4). The advantage however is that this step only needs to be completed once for a given fibre morphology in which the diameters may be varied.
2. If the fibre to be simulated is not at a *DF* value used in step 1, interpolate to determine m_{Vk} as a function of V_{mem} for the *DF* value used as explained in section 2.5v. *DF* is calculated as explained in section 2.1.
3. Calculate SF_{DF} at the *DF* used in the simulation with Eq. (10).
4. Prior to the start of, for example, 100 iterations to determine the discharge probability at a given stimulus level, generate an I_{noise0} matrix using Eq. (4) with k_{fact} = 1 which then contains an initialised current value for each node in 1 μs intervals over the total simulation period.
5. Implement the algorithm in Fig. 4 into the numeric SDE solver. For each step or at each point in time within the sde solver and for each node *n* calculate:
   i. $V_{mem,n}$ from V_n, which is determined by the HH based compartmental model referred to in section 2.3, using Eq. (2).
   ii. $m_{Vk,n}$ required at $V_{mem,n}$ from the gradient function determined in step 1 or 2.
   iii. V_{rms0} from $V_{mem,n}$ using the VD equation (5).
   iv. $V_{rms,n}$ required via Eq. (6).
   v. $k_{fact,n}$ required by substituting $m_{Vk,n}$ and $V_{rms,n}$ into Eq. (7).
   vi. $I_{noise,n}$ required using Eq. (8) by multiplying the initialised $I_{noise0,n}$ value by $k_{fact,n}$ and SF_{DF}.
   vii. The sum of $I_{noise,n}$ and $I_{ion,n}$ as in Eq. (1) to complete the current noise algorithm.

REFERENCES

Briaire JJ, Frijns JHM (2005) Unraveling the electrically evoked compound action potential Hearing Research 205:143-156 doi:10.1016/j.heares.2005.03.020

Bruce IC, Irlicht LS, White MW, O'Leary SJ, Dynes S, Javel E, Clark GM (1999a) A stochastic model of the electrically stimulated auditory nerve: pulse-train response Biomedical Engineering, IEEE Transactions on 46:630-637 doi:10.1109/10.764939

Bruce IC, White MW, Irlicht LS, O'Leary SJ, Dynes S, Javel E, Clark GM (1999b) A stochastic model of the electrically stimulated auditory nerve: single-pulse response Biomedical Engineering, IEEE Transactions on 46:617-629 doi:10.1109/10.764938

Cartee LA (2000) Evaluation of a model of the cochlear neural membrane. II: Comparison of model and physiological measures of membrane properties measured in response to intrameatal electrical stimulation Hearing Research 146:153-166 doi:http://dx.doi.org/10.1016/S0378-5955(00)00110-6

Dangerfield CE, Kay D, Burrage K (2012) Stochastic models and simulation of ion channel dynamics Procedia Computer Science 1:1587-1596 doi:http://dx.doi.org/10.1016/j.procs.2010.04.178

Frijns JHM, Briaire JJ, Grote JJ (2001) The importance of human cochlear anatomy for the results of modiolus-hugging multichannel cochlear implants Otology and Neurotology 22:340-349

Frijns JHM, de Snoo SL, Schoonhoven R (1995) Potential distributions and neural excitation patterns in a rotationally symmetric model of the electrically stimulated cochlea Hearing Research 87:170-186 doi:10.1016/0378-5955(95)00090-q

Frijns JHM, Mooij J, ten Kate JH (1994) A quantitative approach to modeling mammalia myelinated nerve fibers for electrical prostheis design IEEE Transaction on Biomedical Engineering 41:556-566

Goldwyn JH, Shea-Brown E (2011) The what and where of adding channel noise to the Hodgkin-Huxley equations PLoS computational biology 7:e1002247 doi:10.1371/journal.pcbi.1002247

Hales JP, Lin CSY, Bostock H (2004) Variations in excitability of single human motor axons, related to stochastic properties of nodal sodium channels Journal of Physiology 559:953-964

Hanekom T (2001) Three-dimensional spiraling finite element model of the electrically stimulated cochlea Ear and Hearing 22:300-315

Hodgkin AL, Huxley AF (1952) A quantitative description of membrane current and its application to conduction and excitation in nerve Journal of Physiology 117:500-544

Horton AJ (1987) Thermal Noise and Biological Information The Quarterly Review of Biology 62:141-152 doi:10.2307/2829216

Huang Y, Rüdiger S, Shuai J (2013) Langevin approach for stochastic Hodgkin–Huxley dynamics with discretization of channel open fraction Physics Letters A 377:3223-3227 doi:http://dx.doi.org/10.1016/j.physleta.2013.10.008

Izhikevich EM (2004) Which model to use for cortical spiking neurons? Neural Networks, IEEE Transactions on 15:1063-1070 doi:10.1109/tnn.2004.832719

Javel E, Tong YC, Shepherd RK, Clark GM (1987) Responses of cat auditory nerve fibers to biphasic electrical current pulses Annals of Otology, Rhinology & Laryngology 96:26-30

Jönsson R (2010) Field interactions in the peripheral auditory neural system with reference to cochlear implants. Doctoral Thesis, University of Pretoria

Kalkman RK, Briaire JJ, Dekker DM, Frijns JH (2014) Place pitch versus electrode location in a realistic computational model of the implanted human cochlea Hear Res 315C:10-24 doi:10.1016/j.heares.2014.06.003

Macherey O, Carlyon RP, Van Wieringen A, Wouters J (2007) A dual-process integrator-resonator model of the electrically stimulated human auditory nerve JARO - Journal of the Association for Research in Otolaryngology 8:84-104

Malherbe TK, Hanekom T, Hanekom JJ (2013) Can subject-specific single-fibre electrically evoked auditory brainstem response data be predicted from a model? Medical Engineering & Physics 35:926-936 doi:http://dx.doi.org/10.1016/j.medengphy.2012.09.001

Malherbe TK, Hanekom T, Hanekom JJ (2015) The effect of the resistive properties of bone on neural excitation and electric fields in cochlear implant models Hearing Research 327:126-135 doi:10.1016/j.heares.2015.06.003

Manwani A, Steinmetz PN, Koch C (2000) Channel Noise in Excitable Neuronal Membranes. In: Solla SA, Leen TK, Muller KR (eds) Advances in Neural Information Proceedings, 1999. MIT Press, pp 143-149

Mino H, Rubinstein J, White J (2002) Comparison of Algorithms for the Simulation of Action Potentials with Stochastic Sodium Channels Annals of Biomedical Engineering 30:578-587 doi:10.1114/1.1475343

Rattay F (1989) Analysis of models for extracellular fiber stimulation IEEE Transaction on Biomedical Engineering 36:676-682

Rattay F (1990) Electrical Nerve Stimulation, Theory, Experiments and Applications. 1 edn. Springer, Vienna

Rattay F, Leao RN, Felix H (2001a) A model of the electrically excited human cochlear neuron. II. Influence of the three-dimensional cochlear structure on neural excitability Hearing Research 153:64-79 doi:10.1016/s0378-5955(00)00257-4

Rattay F, Lutter P, Felix H (2001b) A model of the electrically excited human cochlear neuron: I. Contribution of neural substructures to the generation and propagation of spikes Hearing Research 153:43-63 doi:10.1016/s0378-5955(00)00256-2

Rattay F, Potrusil T, Wenger C, Wise AK, Glueckert R, Schrott-Fischer A (2013) Impact of Morphometry, Myelinization and Synaptic Current Strength on Spike Conduction in Human and Cat Spiral Ganglion Neurons PLoS ONE 8:e79256 doi:10.1371/journal.pone.0079256

Rubinstein JT (1995) Threshold fluctuations in an N sodium channel model of the node of Ranvier Biophysical journal 68:779-785

Shepherd RK, Javel E (1997) Electrical stimulation of the auditory nerve. I. Correlation of physiological responses with cochlear status Hearing Research 108:112-144 doi:10.1016/s0378-5955(97)00046-4

Sigworth FJ (1980) The variance of sodium current fluctuations at the node of Ranvier Journal of Physiology 307:97-129

Smit JE, Hanekom T, Hanekom JJ (2008) Predicting action potential characteristics of human auditory nerve fibres through modification of the Hodgkin-Huxley equations South African Journal of Science 104:284-292

Smit JE, Hanekom T, Hanekom JJ (2009) Estimation of stimulus attenuation in cochlear implants Journal of Neuroscience Methods 180:363-373

Smit JE, Hanekom T, van Wieringen A, Wouters J, Hanekom JJ (2010) Threshold predictions of different pulse shapes using a human auditory nerve fibre model containing persistent sodium and slow potassium currents Hearing Research 269:12-22 doi:10.1016/j.heares.2010.08.004

Verveen AA (1962) Axon diameter and fluctuation in excitability Acta Morphologica Neerlando-Scandinavica 5:79-85

Verveen AA, Derksen HE (1968) Fluctuation phenomena in nerve membrane Proceedings of the IEEE 56:906-916 doi:10.1109/proc.1968.6443